

Distribution Category: Atomic,
Molecular, and Chemical Physics
(UC-411)

ARGONNE NATIONAL LABORATORY
9700 South Cass Avenue
Argonne, Illinois 60439

ANL/APS/TB-33

Undulator A Diagnostics at the Advanced Photon Source

P. Ilinski

Experimental Facilities Division
Advanced Photon Source

January 1998

work sponsored by
U.S. DEPARTMENT OF ENERGY
Office of Energy Research

TABLE OF CONTENTS

List of Tables	iv
List of Figures	iv
1. Introduction.....	1
2. Diagnostics Setup and Experimental Conditions	1
2.1. Setup	1
2.2. Spectrometer Energy Calibration	2
2.3. Storage Ring Lattice Parameters	2
3. Undulator Diagnostics Results	4
3.1. Undulator Deflection Parameter Value	4
3.2. Radiation Source Position	4
3.3. Particle Beam Divergence.....	7
3.4. Absolute Flux	9
4. Conclusions.....	12
References.....	14

LIST OF TABLES

	page
Table 1. Standard lattice. Designed and measured beta functions, corresponding β_0 values and β_0 locations	15
Table 2. Low-beta lattice. Designed and measured beta functions, corresponding β_0 values and β_0 locations.....	15
Table 3. Position of the effective source.....	16
Table 4. Effective source-to-slit distance	16
Table 5. Rms particle beam divergence.....	16
Table 6. Undulator harmonics FWHM [eV]. Calculated :US - ideal magnetic field, UR - measured magnetic field; emittance included.....	17
Table 7. Relative undulator harmonic flux intensity [%]. Calculated: US - ideal magnetic field, UR - measured magnetic field; emittance included	17
Table 8. Range and rms values of the errors contribution to the flux measurement.....	17

LIST OF FIGURES

Figure 1. Crystal spectrometer calibration: Zn K-edge (9659 eV).....	18
Figure 2. Crystal spectrometer calibration: Zr K-edge (17998 eV).....	18
Figure 3. Measured (solid) first undulator harmonic at a gap of 18.5 mm compared to those calculated for $K=1.217$ (dots) and $K=1.228$ (dashed).....	19
Figure 4. Angular distribution of the $\sin^2(x)/x^2$ function at the first undulator harmonic fundamental energy $E_I(\theta=0)$ (solid), and at the detuned energy: $E_I(1-0.3/N)$ (dots), and $E_I(1-1/N)$ (dashed), $N=70$	19
Figure 5. Measured vertical profiles at 7.3 keV (first harmonic, 18.5 mm gap) at the distances: 27 m (dashed), 28 m (solid), measured (dots).....	20
Figure 6. Measured horizontal profiles at 7.3 keV (first harmonic, 18.5 mm gap), peaks differ for the standard lattice (dashed) by 7%, low-beta lattice (solid) - 4%.....	20
Figure 7. Measured vertical profiles at 7.3 keV (first harmonic, 18.5 mm gap), peaks differ for the standard lattice (dashed) by 7%, low-beta lattice (solid) - 1%.....	21
Figure 8. Measured horizontal profiles at 14.5 keV (second harmonic, 18.5 mm gap), peaks differ for the standard lattice (dashed) by 0.7%, low-beta lattice (solid).....	21

Figure 9.	Calculated vertical profiles at energy 7.3 keV, $\sigma_h = 300 \mu\text{m}$, $\sigma_h' = 24 \mu\text{rad}$, $\sigma_v = 40 \mu\text{m}$, for different rms beam divergences: $\sigma_v' = 2.5$ (dash-dot), 3.0 (solid), 4.0 (dots), 5.0 (dash) μrad	22
Figure 10.	Calculated vertical profiles at energy 7.3 keV, $\sigma_h = 300 \mu\text{m}$, $\sigma_h' = 24 \mu\text{rad}$, $\sigma_v' = 2.5 \mu\text{rad}$, for different rms beam sizes: $\sigma_v = 20$ (dash), 40 (solid), 60 (dots) μm	22
Figure 11.	Horizontal profiles at 14.5 keV (second harmonic), standard lattice. Measured (dots) and calculated for $\sigma_h = 300 \mu\text{m}$, $\sigma_h' = 24.0 \mu\text{rad}$ (solid).	23
Figure 12.	Vertical profiles at 7.3 keV (first harmonic) standard lattice. Measured (dots), calculated for $\sigma_v = 50 \mu\text{m}$, $\sigma_v' = 3.9 \mu\text{rad}$ (solid).....	23
Figure 13.	Horizontal profiles at 14.50 keV (second harmonic), low-beta lattice. Measured (dots), calculated for $\sigma_h = 300 \mu\text{m}$, $\sigma_h' = 22.5 \mu\text{rad}$ (solid).....	24
Figure 14.	Vertical profiles at 7.3 keV (first harmonic) low-beta lattice. Measured (dots), calculated for $\sigma_v = 50 \mu\text{m}$, $\sigma_v' = 5.9 \mu\text{rad}$ (solid).....	24
Figure 15.	A single particle undulator spectrum calculation for the measured magnetic field and different horizontal directions [0.0 mm (dots), 0.2 mm (solid), 0.3 mm (dashed)] at 28 m. The undulator radiation axis corresponds to the maximum intensity and higher harmonic energy value, which is at 0.2 mm (solid).....	25
Figure 16.	Measured undulator absolute flux of the first harmonic at gaps of 18.0 (dot), 18.5 (solid), 19.0 (dashed), through the 150 x 75 μm aperture at 28.0 m.....	25
Figure 17.	Undulator first harmonic absolute flux at the gap of 18.5 mm. Measured (solid), calculated through the 150 x 75 μm aperture at 28.0 m for $\sigma_h = 300 \mu\text{m}$, $\sigma_h' = 24.0 \mu\text{rad}$, for $\sigma_v = 50 \mu\text{m}$, $\sigma_v' = 3.9 \mu\text{rad}$: ideal (dots), measured mag. field and zero energy spread (dashed-dot), measured mag. field and 0.085% energy spread (dashed).....	26
Figure 18.	Undulator third harmonic absolute flux at the gap of 18.5 mm. Measured (solid), calculated through the 150 x 75 μm aperture at 28.0 m for $\sigma_h = 300 \mu\text{m}$, $\sigma_h' = 24.0 \mu\text{rad}$, for $\sigma_v = 50 \mu\text{m}$, $\sigma_v' = 3.9 \mu\text{rad}$: ideal (dots), measured mag. field and zero energy spread (dashed-dot), measured mag. field and 0.085% energy spread (dashed).....	26
Figure 19.	Undulator fifth harmonic absolute flux at the gap of 18.5 mm. Measured (solid), calculated through the 150x75 μm aperture at 28.0 m for $\sigma_h = 300 \mu\text{m}$, $\sigma_h' = 24.0 \mu\text{rad}$, for $\sigma_v = 50 \mu\text{m}$, $\sigma_v' = 3.9 \mu\text{rad}$: ideal (dots), measured mag. field and zero energy spread (dashed-dot), measured mag. field and 0.085% energy spread (dashed).....	27
Figure 20.	Measured on-axis absolute flux density of the first harmonic at a gap of 18.5 mm for the standard lattice (dashed) and low-beta lattice (solid).....	27

Undulator A Diagnostics at the Advanced Photon Source

P. Ilinski

1. Introduction

Diagnostics of Undulator A#2 (UA2) radiation was performed during the October 1997 run at the Advanced Photon Source (APS). The UA2 undulator is a standard 3.3-cm-period APS Undulator A [1], which was positioned downstream from the center of the straight section at Sector 8. The diagnostics included the angular-spectral measurements of the undulator radiation to determine the undulator radiation absolute spectral flux and the particle beam divergence. The results of the absolute spectral flux measurements are compared to the undulator spectrum calculated from measured undulator magnetic field. The particle's energy spread was determined from spectra comparison.

Previously, we reported the first measurements made on Undulator A at the APS [2, 3]. The purpose of the present report is to summarize the results of the diagnostics performed on the Sector 8 undulator at the request of the IMM-CAT staff, and to present a more general discussion of undulator radiation sources at the APS and details of their diagnostics.

2. Diagnostics Setup and Experimental Conditions

2.1. Setup

The undulator diagnostics setup included a pinhole slit assembly to reduce the incident power and to define the angular acceptance and a crystal spectrometer for absolute spectral flux measurements [2]. All components were mounted on a standard APS optical table with five degrees of freedom, so that the setup axis could be adjusted to the axis of the undulator radiation and transverse scans could be performed. The setup was installed in the first optical enclosure (FOE) after two $2 \times 250 \mu\text{m}$ Be windows. The setup entrance slits were $150 \mu\text{m}$ horizontal by $75 \mu\text{m}$ vertical, positioned at 28.0 m from the undulator center and 29.25 m from the center of the straight section. A single-crystal spectrometer combined a Si(111) crystal monochromator and two ion chambers to measure the intensity of the reflected beam. The ion chambers had a 100-mm active path and were filled with a nitrogen gas, whose pressure and temperature were monitored. The use of the second ion

chamber allows one to double-check the ion chamber efficiency and to minimize the background due to the fluorescent scattering from the crystal. The current measurements of the second chamber were used to deduce the absolute flux value. The beam path from the Be window to the crystal was kept in a He atmosphere. An exit window and the ion chamber windows were 25- μm -thick Kapton. A program for data handling and analysis was written using the IGOR C-like language [4].

2.2. Spectrometer Energy Calibration

The undulator deflection parameter can be determined from the undulator harmonic energy position. Comparison of the measured and calculated undulator transverse profiles also requires precise knowledge of the spectrometer energy.

The energy scale of the crystal spectrometer was calibrated using K-edges: Ni (8333 eV), Zn (9659 eV), Ge (11103 eV) and Zr (17998 eV). The results of the calibration with Zn and Zr are shown in Figure 1 and Figure 2. In the energy range from 7 to 20 keV, the spectrometer absolute energy scale was accurate within 15 eV. Energy calibration was repeated every shift and was found reproducible within 2 eV.

2.3. Storage Ring Lattice Parameters

The storage ring lattice parameters define the particle beam size and divergence, which greatly affect an undulator radiation spectrum. The beam size and divergence can be obtained at any point of the storage ring by knowing the beam emittance, and the alpha, beta and dispersion functions [5]. Undulators are installed in the straight sections of the storage ring, where the alpha and the dispersion function are zero at the APS, and the particle beam will be fully characterized by the beam emittance, ϵ , and the beta function, β . The vertical emittance can be minimized by adjusting lattice parameters and may be less than 5% of the horizontal emittance value.

A particle beam in a well-behaved storage ring has a Gaussian distribution in the phase space and can be represented by a sigma contour that is the phase ellipse [5]. At the location where the beta function is minimal, β_o , the maximum rms beam source size and divergence are equal to $\sigma_o = \sqrt{\epsilon\beta_o}$ and $\sigma'_o = \sqrt{\epsilon/\beta_o}$, respectively, and the beam phase ellipse is upright.

The resulting undulator radiation is a convolution of the undulator radiation emitted by one particle and the particle beam. The range of the β_o value deviations will determine

the range of the beam source size and divergence changes, which will change the maximum radiation intensity. At the APS, the β_0 location defines mainly the position of the source (see Section 3.2). Therefore the variation of the β_0 location will change the distance to the source.

The beta function measurements were performed by the Accelerator System Division (ASD) at the APS. The results of the measurements showed that the value of the beta function at the quadrupoles SXXB:Q1 and SX(X+1)A:Q1, which are at the beginning and the end of the straight section, may vary from the design value and may not be equal [6]. In the case that they are not equal, the location of the minimum beta function will be away from the center of the straight section.

The beta function in the straight section, that is free space, has the form $\beta(z) = \beta_0 + z^2 / \beta_0$, where z is the distance from the β_0 location. The minimum value of the beta function and its position can be calculated by knowing values of the beta function at the beginning and at the end of the straight section and the beta function form, $\beta(z)$. The ASD beta function measurements were made at the centers of the SXXB:Q1 and SXXA:Q1 quadrupoles, which are 0.5 m long. The beta function values can be evaluated at the end and the beginning of the quadrupoles, which correspond to the beginning and the end of the straight section. The distance between the SXXB:Q1 quadrupole end and the beginning of the SX(X+1)A:Q1 quadrupole is equal to 6.72 m and defines the optical length of the straight section.

The beta function measurements were made for a standard APS storage-ring lattice (designed beta functions) and for a lattice with a low vertical beta function configuration [6]. The beta function measured at the quadrupole's centers, and those evaluated at the beginning and at the end of the straight section, and the calculated corresponding β_0 values and locations are given in Table 1 for Sectors 2, 3 and 8 for the standard APS lattice. The same parameters for Sectors 35 and 36 are summarized in Table 2 for the low-beta lattice configuration. As can be seen from these tables, the β_0 values vary from the design specification as much as 20%, and the position may be up to 1.8 m away from the center of the straight section.

The beta function measurements were performed at Sector 8 for the standard lattice configuration on 11/17/97, after the undulator diagnostics was completed. The measured β_0 value at Sector 8 and its location are close to the design specifications.

3. Undulator Diagnostics Results

To evaluate undulator performance, the measured undulator flux has to be compared to the calculated flux. The angular spectral characteristics for an ideal undulator with sinusoidal magnetic field were calculated using the program US [7]. Spectral flux of the real undulator was calculated for a particular undulator from the measured magnetic field [8] by use of the program UR [9]. The undulator radiation flux calculations require knowledge of the undulator deflection parameter value, distance to the source, slit sizes, and particle beam parameters: horizontal and vertical rms beam size and divergence. To make a reasonable comparison between flux calculations and absolute flux measurements, the accuracy of these parameters should be known at least to the same order of magnitude as the accuracy of the absolute flux measurements itself. Individual error contributions to the absolute flux measurements are discussed in Section 3.4.

3.1. Undulator Deflection Parameter Value

For an ideal sinusoidal trajectory, the undulator deflection parameter K is interpreted as the maximum deflection angle in units of $1/\gamma$, $K = 0.934\lambda_u[cm]B_o[T]$. An effective K value of 1.217 was determined from the UA2 magnetic measurements at a gap of 18.5 mm [10]. The measured peak magnetic field at a gap of 18.5 mm was 3.95 ± 0.02 T.

A spectrum of the first undulator harmonic measured at a gap of 18.5 mm is shown in Figure 3; it is compared to that calculated for an ideal undulator with an undulator deflection parameter value of $K=1.217$. The two spectra differ by an energy distance of 60 eV, indicating that the actual K value at the given gap size is larger than 1.217. The K value that corresponds to the measured spectrum was found to be 1.228, which is demonstrated by the match of the measured and calculated undulator spectrums for $K=1.228$ (Figure 3). The larger K value could be due to the higher peak magnetic field by a factor of 40 Gauss or by a 94 μm smaller gap size, corresponding to a 18.406 mm gap. The exact reasons for the K value discrepancy have to be investigated.

3.2. Radiation Source Position

To calculate the undulator radiation flux, one must know the distance from the setup entrance slits to the radiation source. Photons emitted by particles traveling along the undulator form a real source. We will call the radiation emitted by one particle the intrinsic undulator radiation. The resulting undulator radiation is a convolution of the intrinsic

undulator radiation and the particle beam. The increased total angular spread, due to the convolution, will form an effective source. In the case of no divergence introduced by the undulator, the effective source position will be at the location at which the particle beam phase ellipse is upright, that is the β_0 location. When the intrinsic undulator divergence cannot be neglected, the effective source position will not coincide with the β_0 location.

A phase space representation can be used to obtain the effective source position [11]. The particle beam has a Gaussian distribution in the phase space; it can be characterized by the sigma contour that is the phase ellipse. After translation from the upright phase ellipse position, the β_0 location, to the center of the undulator, which is at distance L , the particle beam phase ellipse will take the form:

$$\begin{pmatrix} 1 & L \\ 0 & 1 \end{pmatrix} \begin{pmatrix} \sigma_o & 0 \\ 0 & \sigma'_o \end{pmatrix} = \begin{pmatrix} \sigma_o & L\sigma'_o \\ 0 & \sigma'_o \end{pmatrix}.$$

The choice of the undulator center as the nominal position of the real source is acceptable for the on-axis flux calculation in the far field zone. In this case, the error in averaging of the aperture solid angle is small.

At the nominal position of the real source, the particle beam phase ellipse will be convoluted with the intrinsic undulator radiation phase ellipse. The intrinsic undulator radiation phase ellipse is represented by the intrinsic undulator source size and divergence. The source size of the intrinsic undulator radiation in the x-ray energy range is much smaller than the particle beam size and can be neglected. The angular distribution of the intrinsic undulator radiation is characterized in the first approximation by the $\sin^2(x)/x^2$ function. For the on-axis radiation at the fundamental harmonic energy, $E_1(\theta=0)$, the intrinsic undulator radiation divergence can be approximated by a Gaussian distribution with the rms divergence equal to $\sigma'_u = 1/2\gamma\sqrt{(1 + K^2/2)nN}$ [12], where n is the harmonic number, and N is the number of undulator periods. The convolution of the beam phase ellipse with the intrinsic undulator radiation phase ellipse will result in a new phase ellipse:

$$\begin{pmatrix} \sigma_o & L\sigma'_o \\ 0 & \sqrt{\sigma_o'^2 + \sigma_u'^2} \end{pmatrix}.$$

To obtain the effective source position, we transform the convoluted ellipse back by a distance X :

$$\begin{pmatrix} 1 & -X \\ 0 & 1 \end{pmatrix} \begin{pmatrix} \sigma_o & L\sigma'_o \\ 0 & \sqrt{\sigma_o'^2 + \sigma_u'^2} \end{pmatrix} = \begin{pmatrix} \sigma_o & L\sigma'_o - X\sqrt{\sigma_o'^2 + \sigma_u'^2} \\ 0 & \sqrt{\sigma_o'^2 + \sigma_u'^2} \end{pmatrix}.$$

The effective source position corresponds to the location at which the convoluted ellipse is upright. The upright ellipse position is at the point where there is no ellipse tilting, resulting in:

$$L\sigma'_o - X\sqrt{\sigma_o'^2 + \sigma_u'^2} = 0.$$

The distance from the nominal position of the real source to the effective source position,

$$X = \frac{L}{\sqrt{1 + \frac{\sigma_u'^2}{\sigma_o'^2}}},$$

depends on the ratio of the undulator intrinsic divergence to the particle beam divergence. The calculated distances X , and $(L - X)$, that is the distance from the β_o location to the effective source position, are presented in Table 3. The distance L of 1260 mm between the undulator center and the β_o location was used, which corresponds to the β_o location at the center of the straight section. The calculation was made for the first harmonic with $K=1.228$, which has the rms intrinsic divergence of $5.8 \mu\text{rad}$. In the horizontal direction, the beam divergence is dominating over the undulator intrinsic divergence, and the effective source position is close to the β_o location. In the vertical direction, the undulator intrinsic divergence is comparable to the beam divergence, and the effective source position is 0.55 m away from the β_o location.

The above approach for defining the effective source position is based on knowledge of the β_o location; it demonstrates that the ratio of the undulator intrinsic divergence to the particle beam divergence finally determines the effective source position. The β_o location can vary during the run, so determination of the effective source position by means of the above method may be not reliable.

Another approach to determine the effective source position is based on the measurements of the undulator beam transverse profile at the detuned harmonic energy, which is less than the fundamental harmonic energy, $E_f(\theta=0)$. As was mentioned above,

the radial angular distribution of the undulator radiation is characterized by the $\sin^2(x)/x^2$ function, where $x=\pi N((E-nE_1)/E_1)$ is the function of angle and energy, n is the harmonic number, N is the number of undulator periods, and $E_1=E_1(\theta,K)$ is the energy of the first harmonic. The angular distribution at the detuned energy has the shape of a hollow cone; the profile peaks appear at a particular angle for a given detuned energy. Figure 4 demonstrates the $\sin^2(x)/x^2$ function angular distribution at the fundamental harmonic energy, $E_1(\theta=0)$, and at two detuned harmonic energies. Two vertical profiles of the first harmonic calculated at 7.3 keV for an ideal undulator at distances of 27 and 28 m are compared to a measured vertical profile in Figure 5.

The distances to the source were obtained from fitting the calculated profile to the measured profile by varying the distance. In reality, the distance to the source and the beam divergences are obtained simultaneously during the transverse profile's fitting. The source-to-slit distances obtained by the two methods are summarized in Table 4. For the standard lattice, the distance from the slits to the source was determined to be of 28.2 m in the vertical direction and 28.0 m in the horizontal direction. The distance of 28.0 m coincides with the undulator center. The value of horizontal distance has to be used for the flux calculations because the horizontal beam divergence dominates over the vertical beam divergence when a two-dimensional convolution is performed. For the low-beta lattice configuration, the distance to the source was found to be 27.6 m in the horizontal direction and 28.3 m in the vertical. The distance of 27.6 m was used for the flux calculations. The horizontal distances determined from the profile measurement are smaller than the vertical distances, indicating that during the measurements the β_0 location was downstream from the undulator center. The beta function measurements at Sector 8 for the standard lattice configuration, presented in Table 1, showed an upstream β_0 location shift of 0.2 m, but those measurements were not performed at the same time as the undulator diagnostics.

3.3. Particle Beam Divergence

Particle beam divergence can be determined from the undulator radiation transverse profiles. The profiles were recorded at the detuned harmonic energy, where the angular distribution of the undulator radiation is characterized by a hollow cone (Figure 4). The angular width of the peaks at the detuned energy is smaller than at the fundamental harmonic energy, when the maximum intensity is on-axis. Analysis shows that the minimum width of the peaks occurs at a detuned energy of $E_n/2$, corresponding to a $1/\gamma$

off-axis angle, but the intensity of the peaks is very small. Therefore a compromise is made: the detuned energy has to be chosen so that the width of the maximum is smaller than the beam divergence and the signal-to-background ratio is high. Recording the angular distribution at the detuned harmonic energy allows one to improve the accuracy of the beam divergence measurements, because the beam divergence dominates over the undulator intrinsic divergence. That is especially important for the vertical beam divergence measurements at the APS, where the vertical beam divergence can be smaller than the undulator intrinsic divergence at the fundamental harmonic energy.

The measured angular distributions of the undulator radiation at the detuned energy were slightly asymmetrical, which complicated the beam divergence determination. When the angular distributions were measured at the detuned energy (7.3 keV) of the first harmonic, the standard lattice configuration peaks differed by 7% for both the horizontal and vertical directions, Figure 6 and Figure 7. The peak's difference for the low-beta lattice was 4% for horizontal measurements and 1% for vertical (Figure 6, Figure 7). There was less asymmetry in the horizontal direction for both lattice configurations at the detuned energy (14.5 keV) of the second harmonic: 0.7% for the standard lattice and no asymmetry for the low-beta lattice (Figure 8). From the fact that the asymmetry changes for different lattice configurations, it is possible to assume that the asymmetry of the profiles is due to the particle beam and is not caused by the nature of the undulator magnetic field.

The horizontal and vertical particle beam divergences were derived by fitting the calculated profiles to the measured transverse profiles. The program US was used to calculate the transverse distribution; the variable parameters were the rms beam divergence, the rms beam size, and the distance to the source. The distance can be considered as an independent parameter that defines the separation between profile peaks, but the beam divergence and beam size parameters are coupled. The transverse profile at a distance z is a convolution of the undulator radiation with the particle beam that can be represented by a Gaussian distribution with rms size equal to the $\sqrt{\sigma^2 + (z\sigma')^2}$. The beam size can be obtained from independent measurements or estimated if the β_0 value and position are known. If the beam size is not known precisely, the uncertainty introduced by the undefined rms beam size will decrease with distance. For profiles measured at 28 m, a $\pm 50 \mu\text{m}$ uncertainty in the rms horizontal beam size will give a $\pm 0.9 \mu\text{rad}$ uncertainty for the horizontal rms angular divergence, and a $\pm 20 \mu\text{m}$ uncertainty in the rms vertical beam size will give a $\pm 0.3 \mu\text{rad}$ uncertainty for the vertical rms angular divergence. The influence of the beam angular divergence parameter on the vertical profile is shown in Figure 9, where

vertical profiles calculated at 7.3 keV energy for different rms beam angular divergences (2.5, 3, 4, 5 μrad , and for a 40 μm beam size) are shown. The results of calculations for different rms beam sizes (20, 40, 60 μm , and for a 4 μrad rms beam divergence) are plotted in Figure 10.

The azimuthal distribution of the planar undulator radiation at the detuned harmonic energy is anisotropic. This property was used to define the best experimental condition combination for the divergence measurements. The vertical profile of the first undulator harmonic was used to determine the vertical beam divergence. The horizontal profile of the second undulator harmonic was used to determine the horizontal beam divergence. The vertical profiles were measured at energy of 7.3 keV, while the maximum of the first harmonic was at 7.99 keV (18.5 mm gap). The horizontal profiles were measured at 14.5 keV, with the maximum of the second harmonic at 15.4 keV (18.5 mm gap). The results are summarized in Table 5 and are shown for the standard lattice in Figure 11 and Figure 12 and for the low-beta lattice in Figure 13 and Figure 14.

3.4. Absolute Flux

To evaluate the undulator performance, experimental results have to be compared with calculations. Undulator spectral flux was calculated using the program UR from the undulator UA2 magnetic field measured at a gap of 18.5 mm [10]. The undulator horizontal trajectory calculated from the measured magnetic field had a 7- μrad inclination angle with respect to the geometrical undulator axis. To verify the actual direction of the undulator radiation, a set of single particle spectra was calculated, Figure 15. The axis of the radiation corresponds to the spectrum with the maximum intensity and highest harmonic energy. Figure 15 shows that the first harmonic had maximum intensity at 0.2 mm in the horizontal direction at 28 m from the source, this direction was used for the on-axis undulator spectral flux calculation.

A set of the flux measurements performed at gaps of 18.0, 18.5, and 19.0 mm are presented in Figure 16. In Figure 17, Figure 18, and Figure 19 the absolute flux measured at a gap of 18.5 mm is compared with the flux calculated for the ideal undulator and from the measured magnetic field for the first, third, and fifth undulator harmonics, correspondingly. Flux was calculated through the 150 x 75 μm pinhole at distance of a 28 m and with the standard lattice beam parameters determined from the measurements, Table 5. The angular acceptance of the slit aperture was 5.4 μrad (horizontally) by 2.7 μrad (vertically), that is small compared to the full width at half maximum (FWHM) of the measured undulator radiation at the maximum intensity energy of the first harmonic (8.0

keV), which was $62.8 \mu\text{rad}$ (horizontally) by $19.3 \mu\text{rad}$ (vertically); for higher harmonics, the FWHM will be approximately \sqrt{n} times smaller. Thus the angular flux density of the first, third and fifth harmonics can be obtained by dividing the measured flux by the acceptance solid angle. The undulator deflection parameter determined from the measured undulator spectrum was $K=1.228$, while $K=1.217$ corresponded to the undulator magnetic field at a gap of 18.5 mm. To match measured and calculated spectra energy scales, the energy scale of the calculated spectrum was adjusted to a K value of 1.228. The flux difference for $K=1.217$ and $K=1.228$ is less than 0.3% and can be neglected.

The width of the observed undulator harmonics is significantly broader than the intrinsic width of the undulator harmonics, which for the odd harmonics is approximately equal to E_f/N , where N is the number of undulator periods. The broadening is caused by the beam emittance, undulator magnetic field errors, finite-aperture-size, and the particle's energy spread. When calculating the undulator spectrum from the measured magnetic field for a given aperture and beam parameters, the only undefined parameter is the particle's energy spread. Therefore the particle energy spread can be determined by varying the energy spread value while calculating the undulator spectrum until the harmonic width matches the width of the undulator harmonic of the measured spectrum. A particle's energy spread of 0.085% was determined from the fitting of the undulator third harmonic. A comparison of the measured and calculated FWHM of the undulator harmonics is presented in Table 6. For 0.085% particle energy spread, the harmonic width of the calculated first and fifth harmonics does not exactly match the width of the measured undulator harmonics. The calculated FWHM of the fifth harmonic is 330 eV compared to the measured value of 366 eV.

The broadening of the harmonics caused by the presence of the undulator magnetic field errors reduces the harmonic's maximum intensity. Instead of using the rms field error to evaluate the quality of the undulator magnetic field, the rms phase error was introduced as a figure of merit of the undulator spectral performance. The ratio of the undulator harmonic intensity with the rms phase error of σ_ϕ to an ideal undulator harmonic intensity can be estimated as $I_n/I_{n0} \approx \exp(-n^2\sigma_\phi^2)$, where n is the harmonic number [13]. Undulator UA2 has a very small rms phase error value of 3.2 degrees, determined from the undulator magnetic field measurements at a gap of 18.5 mm. The broadening of the harmonics caused by the presence of the beam emittance and the particle's energy spread will additionally reduce the harmonics maximum.

The flux calculated for the measured magnetic field with zero and 0.085% particle energy spread is also plotted in Figure 17, Figure 18, and Figure 19. The relative

intensities of the harmonics are summarized in Table 7. The undulator flux calculated from the magnetic field with the determined beam divergence and with 0.085% particle energy spread was normalized to 100%. As can be seen from Table 7, the measured absolute flux at a gap of 18.5 mm for the first and third harmonics is within 1% of the undulator flux calculated from measured magnetic field, determined beam parameters, and 0.085% energy spread. The measured flux of the fifth harmonic is 15% less than calculated.

The range of the experimental errors and parameters errors and their rms contribution values to the flux measurement and comparison are summarized in Table 8. Error distributions were considered to be flat with the rms value of $\Delta/\sqrt{12}$, where Δ is the range of the error contribution. The total rms value was calculated as a square root of the individual rms square's sum.

The fundamental energy of the first harmonic, $E_1(\theta=0)$, for $K=1.228$ is 8.04 keV; the position of the maximum intensity is shifted by 50 eV and located at 7.99 keV, Figure 17. The energy shift of the maximum intensity is due to the on-axis appearance of the lower energy photons emitted by the off-axis particles. When the spectrum is detected with a pinhole, the energy shift of the maximum intensity is caused by the particle beam angular divergence. The angular divergence effect for the on-axis undulator spectrum is similar to the over-angle integration of the undulator radiation. As was mentioned above, the angular distribution of the undulator radiation in the first approximation can be represented by the $\sin^2(x)/x^2$ function, Figure 4. The over-angle integration of the $\sin^2(x)/x^2$ function will have a maximum at the detuned energy of $E_1(1-1/N)$ [12]. This energy value can be used as a lower limit of the maximum intensity position. An exact shift is smaller because of the Gaussian angular distribution of the particle beam and because the undulator radiation intensity is decreasing when the off-axis angle is increasing. The finite aperture size will produce an additional low energy shift of the intensity maximum. An estimated energy shift of the maximum intensity from the fundamental harmonic energy (8.04 keV) is $E_1/N=115$ eV, and the actual difference was 50 eV.

A comparison of the on-axis flux densities of the first harmonic measured at a gap of 18.5 mm for the standard lattice and the low vertical beta lattice is shown in Figure 20. The harmonic FWHM increased from 178 eV for the standard lattice to 211 eV for the low-beta lattice. The rms vertical divergence increased from 3.9 μ rad for the standard lattice to 5.9 μ rad for the low-beta lattice, while the horizontal divergence decreased from 24 μ rad to 22.5 μ rad because of the larger horizontal beta function (see Table 2). The on-axis flux density decreased to 92% of that for the standard lattice configuration. The flux density did not change significantly because of the horizontal divergence domination over the vertical

when two-dimensional convolution with the particle beam was performed. Nevertheless, the larger vertical divergence for the low-beta lattice could require increasing the size of the vertical aperture of the apparatus to collect the same total photon flux as for the standard lattice case.

4. Conclusions

The results of the undulator UA2 diagnostics showed that the undulator spectrum measured at different gaps (18.0, 18.5, 19.0 mm) is close to what one could expect. At a gap of 18.5 mm, the measured undulator flux is in a good agreement with the calculated flux. Flux calculations were performed with the measured undulator UA2 magnetic field at a gap of 18.5 mm and with the particle beam divergence, particle energy spread, and distance to the source determined from the undulator radiation measurements. Diagnostics were done for the standard storage ring lattice and for the lattice with low vertical beta function.

For the standard lattice, the measured absolute flux for the first and third harmonics at a gap of 18.5 mm was within 1% of the calculated undulator flux. The measured flux of the fifth harmonic was 15% less than calculated.

For the low-beta lattice, on-axis flux density of the first harmonic decreased to 92% of that for the standard lattice configuration. The flux density did not change significantly because the horizontal divergence dominates the vertical when two-dimensional convolution is performed. Nevertheless, the larger vertical divergence for the low-beta lattice configuration could require increasing the size of the vertical aperture of the apparatus to obtain the same total photon flux as for the standard lattice configuration.

Beam divergence was determined from the measured undulator transverse profiles at the detuned harmonic energy, which is less than the fundamental harmonic energy. Measuring angular distribution at the detuned harmonic energy allows one to improve the accuracy of the beam divergence evaluation, because the beam divergence dominates over the intrinsic divergence of the undulator radiation. However, the observed asymmetry of the undulator transverse profiles at the detuned energy may complicate the analysis. From comparison of the profile asymmetries for different storage ring lattice configurations, the assumption was made that the asymmetry effect is due to the nature of the particle beam rather than a property of the undulator.

Undulator transverse profile calculations requires knowing the value of the undulator deflection parameter K , which was determined from the energy position of the measured

first undulator harmonic. The undulator measured deflection parameter at a gap of 18.5 mm was $K=1.228$, which differs from the value $K=1.217$, calculated from the magnetic measurement. The larger K value could be due to the peak magnetic field being higher by 40 Gauss or by the gap size being smaller by 94 μm .

It was found that the undulator second harmonic profile is more sensitive to the horizontal beam divergence changes, and the odd harmonic profiles to the vertical beam divergence. The rms particle beam divergences of $24.0 \pm 0.9 \mu\text{rad}$ (horizontal) and $3.9 \pm 0.3 \mu\text{rad}$ (vertical) were determined for the standard storage ring lattice configuration; $22.5 \pm 0.9 \mu\text{rad}$ (horizontal) and $5.9 \pm 0.3 \mu\text{rad}$ (vertical) for the low-beta configuration. When beam divergence is determined from the transverse profiles, the main source of the systematic error is the inaccuracy of the beam size.

A particle energy spread of 0.085% was determined from fitting the calculated width of the third harmonic to the measured one. For a 0.085% particle energy spread, the harmonic widths of the calculated first and fifth harmonics do not exactly match the measured widths of the undulator harmonics. The calculated FWHM of the fifth harmonic is 330 eV compared to 366 eV for the measured harmonic.

The beta function measurements in the straight section, performed by ASD, have shown that the minimum beta function position, which mainly defines the location of the effective source at the APS, may be up to 2 m away from the center of the straight section. To avoid uncertainty, the distance to the effective source was determined from the undulator transverse profile measured at the detuned harmonic energy, where peaks appear at a particular angle for a given detuned energy.

Acknowledgment

This work was supported by the U.S. Department of Energy, BES-Office of Energy Research, under Contract No. W-31-109-Eng-38. I am grateful to Efim Gluskin for his constant support and critical discussions. I want to acknowledge Brian Tieman and Joe Arko for their technical assistance, Nick Sereno (ASD) for beta function measurements, and Roger Dejus for supporting the US and UR codes. I also would like to thank the Beamline Controls & Data Acquisition Group, Beamline Operation Group, and IMM-CAT (Sector 8) personnel for their cooperation.

References

1. R. J. Dejus, B. Lai, L. Moog, E. Gluskin, Undulator A Characteristics and Specifications: Enhanced Capabilities, *Advanced Photon Source Technical Bulletin ANL/APS/TB-17*, Argonne National Laboratory, May 1994.
2. Z. Cai, R. J. Dejus, P. D. Hartog, Y. Feng, E. Gluskin, D. Haeffner, P. Ilinski, B. Lai, D. Legnini, E.R. Moog, S. Shastri, E. Trakhtenberg, I. Vasserman, W. Yun, APS Undulator Radiation - First Results, *Rev. Sci. Instrum.* **67**, CD ROM (1996).
3. P. Ilinski, R. J. Dejus, E. Gluskin, T. I. Morrison, Some Practical Aspects of Undulator Radiation Properties, Optics for High-Brightness Synchrotron Radiation Beamlines II (SPIE, Denver, Colorado, 1996), v. 2856, pp. 16-25.
4. Igor Pro, WaveMetrics, P.O. Box 2088, Lake Oswego, OR 97035.
5. S. Krinsky, M. L. Perlman, R. E. Watson, in *Handbook on Synchrotron Radiation* E. E. Koch, Ed. (North-Holland Publishing, Amsterdam, 1983), v. 1A, pp. 65-171.
6. N. Sereno, /home/helios/SERENO/tcl/SRApplications/SRBetaMeasDir, *File Directory*, Accelerator System Division, Advanced Photon Source 1997.
7. R. J. Dejus, M. S. d. Rio, A Graphical User Interface for Spectral Calculations and X-ray Optics Utilities, *Rev. Sci. Instrum.* **67**, CD ROM (1996).
8. L. Burkel, R. Dejus, J. Maines, J. O'Brien, J. Pfluger, I. Vasserman, The Insertion Device Magnetic Measurement Facility: Prototype and Operational Procedures, *Advanced Photon Source Technical Bulletin ANL/APS/TB-12*, Argonne National Laboratory, March 1993.
9. R. J. Dejus, A. Luccio, Program UR: General Purpose Code for Synchrotron Radiation Calculations, *Nucl. Instr. and Meth.* **A347**, 61-66 (1994).
10. I. Vasserman, oxygen/pchome/iddata/ua2m/u203061.18, *Data File*, Experimental Facilities Division, Advanced Photon Source, March 1997.
11. G. K. Green, Spectra and Optics of Synchrotron Radiation, *Report BNL-50522*, Brookhaven Nation Labratory 1976.
12. R. Coisson, R. P. Walker, Phase Space Distribution of Brilliance of Undulator Sources, R. Tatchyn, I. Lindaus, Eds., International Conference on Insertion Devices for Synchrotron Radiation (SPIE, Stanford, California, 1985), v. 582, pp. 24-29.
13. R. P. Walker, Interference Effects in Undulator and Wiggler Radiation sources, *Nucl. Instr. and Meth.* **A335**, 328-337 (1993).

Table 1. Standard lattice. Designed and measured beta functions, corresponding β_0 values and β_0 locations

Sector No.	Date of measurement	β center B:Q1 [m]	β str.sect. starts [m]	β center A:Q1 [m]	β str.sect. ends [m]	β_0 [m]	β_0 position from the center of the straight section [m]
	Designed Hor.	15.5	15.0	15.5	15.0	14.2	0.0
2	09/30/97 Hor.	19.4	18.9	18	17.5	17.4	1.8
3	09/30/97 Hor.	17.7	17.2	18.4	17.9	16.8	-0.9
8	11/17/97 Hor.	15.9	15.4	15.7	15.2	14.5	0.2
	Designed Vert.	11.0	11.1	11.0	11.1	10.0	0.0
2	09/30/97 Vert.	7.7	7.8	9.3	9.4	6.7	-0.8
3	09/30/97 Vert.	8.2	8.3	8.4	8.5	6.7	-0.1
8	11/17/97 Vert.	11.6	11.7	11.4	11.5	10.5	0.2

Table 2. Low-beta lattice. Designed and measured beta functions, corresponding β_0 values and β_0 locations

Sector No.	Date of measurement	β center B:Q1 [m]	β str.sect. starts [m]	β center A:Q1 [m]	β str.sect. ends [m]	β_0 [m]	β_0 position from the center of the straight section [m]
	Designed Hor.	17.4	16.7	17.4	16.7	16.0	0.0
35	09/23/97 Hor.	16.9	16.2	17.4	16.7	16.4	-0.6
36	09/23/97 Hor.	16.6	15.9	17.2	16.5	16.2	-0.7
	Designed Vert.	7.1	6.8	7.1	6.8	3.0	0.0
35	09/23/97 Vert.	3.7	3.5	10.8	10.3	-	-
36	09/23/97 Vert.	5.2	5.0	9.5	9.1	3.5	-1.1

Table 3. Position of the effective source

	Undulator intrinsic divergence $K=1.228$ [μrad]	Particle beam divergence [μrad]	Distance from the undulator center to the effective source position, X [m]	Distance from the β_0 location to the effective source position, ($L-X$) [m]	Effective source-to-slit distance [m]
Horizontal	5.8	24	1.22	0.035	29.2
Vertical	5.8	5.9	1.13	0.130	29.1
Vertical	5.8	3.9	0.70	0.550	28.7

Table 4. Effective source-to-slit distance

Method	Lattice configuration	Effective source-to-slit distance [m]		Difference between horizontal and vertical distances [m]
		Horizontal	Vertical	
Calculation	Standard	29.2	29.1	0.1
Calculation	Low-beta	29.2	28.7	0.5
Profile measurement	Standard	28.0	28.2	-0.2
Profile measurement	Low-beta	27.6	28.3	-0.7

Table 5. Rms particle beam divergence

Rms angular divergence [μrad]		
	Standard lattice	Low-beta lattice
Horizontal	24.0 ± 0.9	22.5 ± 0.9
Vertical	3.9 ± 0.3	5.9 ± 0.2

Table 6. Undulator harmonics FWHM [eV]. Calculated: US code - ideal magnetic field, UR code - measured magnetic field; emittance included

Undulator harmonic number		1	3	5
Zero	energy spread (code US)	176	227	233
Zero	energy spread (code UR)	176	230	241
0.1%	energy spread (code UR)	186	288	353
0.085%	energy spread (code UR)	183	274	330
Experiment		178	274	366

Table 7. Relative undulator harmonic flux intensity [%]. Calculated: US code - ideal magnetic field, UR code - measured magnetic field; emittance included

Undulator harmonic number		1	3	5
Zero	energy spread (code US)	103	124	155
Zero	energy spread (code UR)	102	114	126
0.085%	energy spread (code UR)	100	100	100
Experiment		99	101	85

Table 8. Range and rms values of the errors contribution to the flux measurement

Error source	Error range	Contribution to the flux value rms [%]
Experiment		
Filters/air transmission	7%	2
Crystal integrated bandwidth	10%	3
Ion chamber efficiency	7%	2
Beam current	3%	1
Parameter used for spectrum calculation		
Rms particle beam divergence	± 0.9 [μrad]	4
Particle's energy spread	20%	3
Distance to the source	± 1 [m]	2
Slits size	± 2 [μm]	2
Total		6.7

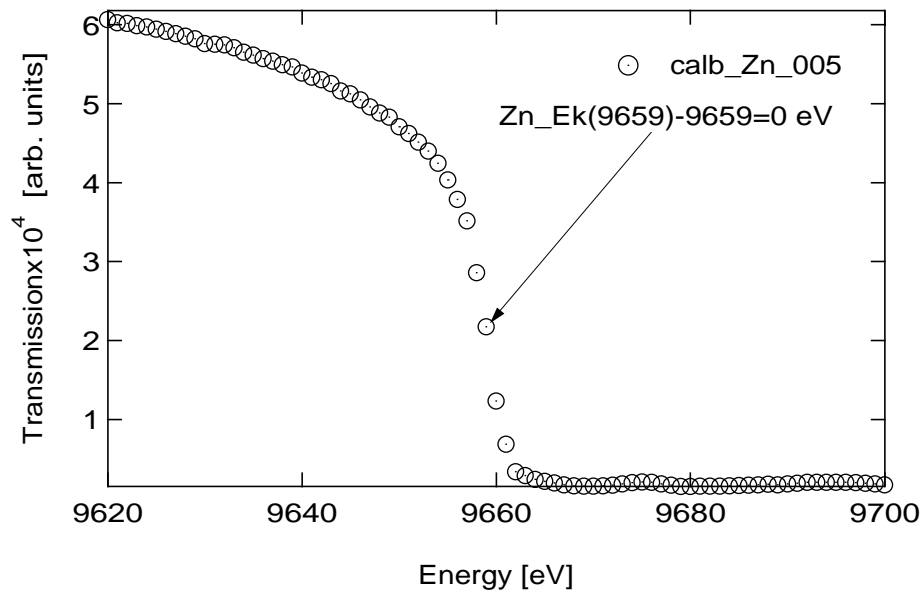


Figure 1. Crystal spectrometer calibration: Zn K-edge (9659 eV).

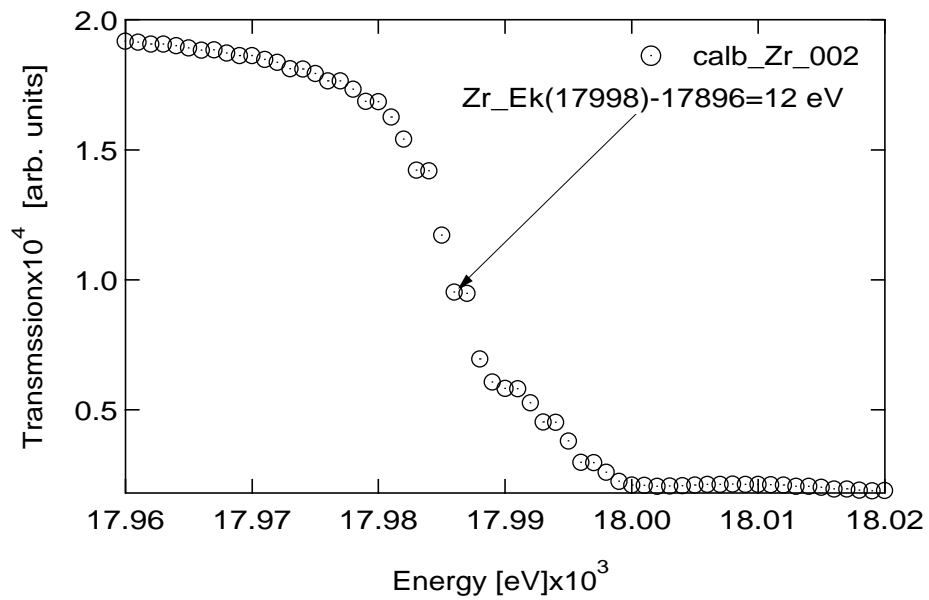


Figure 2. Crystal spectrometer calibration: Zr K-edge (17998 eV).

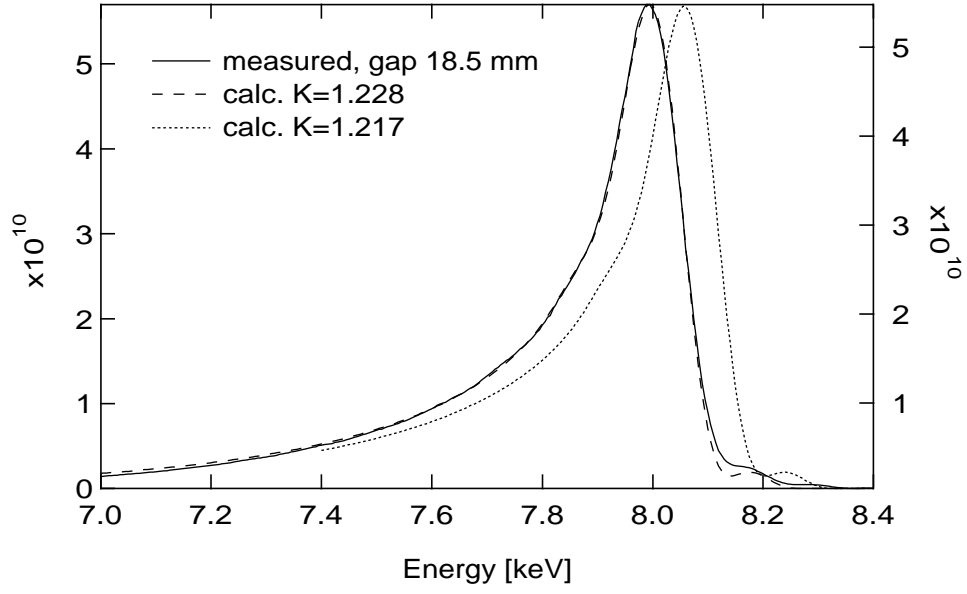


Figure 3. Measured (solid) first undulator harmonic at a gap of 18.5 mm compared to those calculated for $K=1.217$ (dots) and $K=1.228$ (dashed).

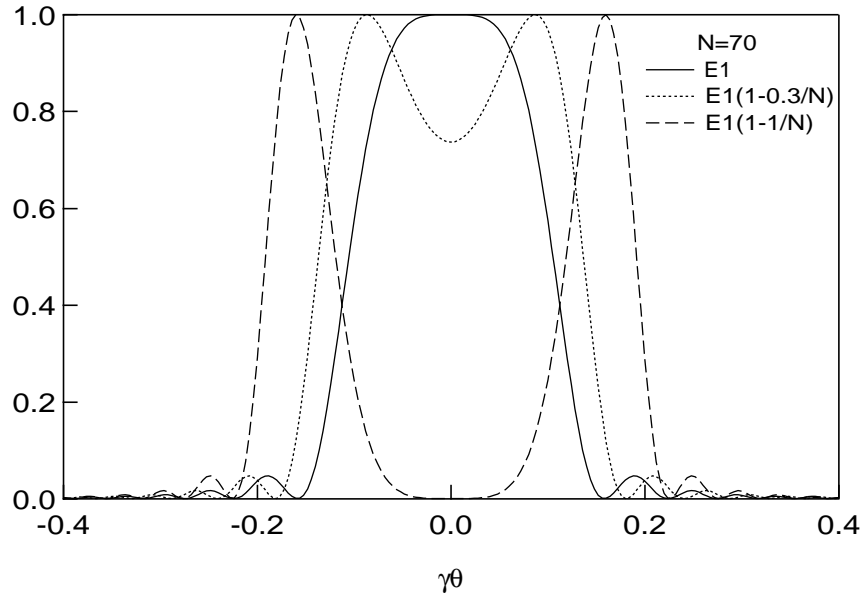


Figure 4. Angular distribution of the $\sin^2(x)/x^2$ function at the first undulator harmonic fundamental energy $E_1(\theta=0)$ (solid), and at the detuned energy: $E_1(1-0.3/N)$ (dots), and $E_1(1-1/N)$ (dashed), $N=70$.

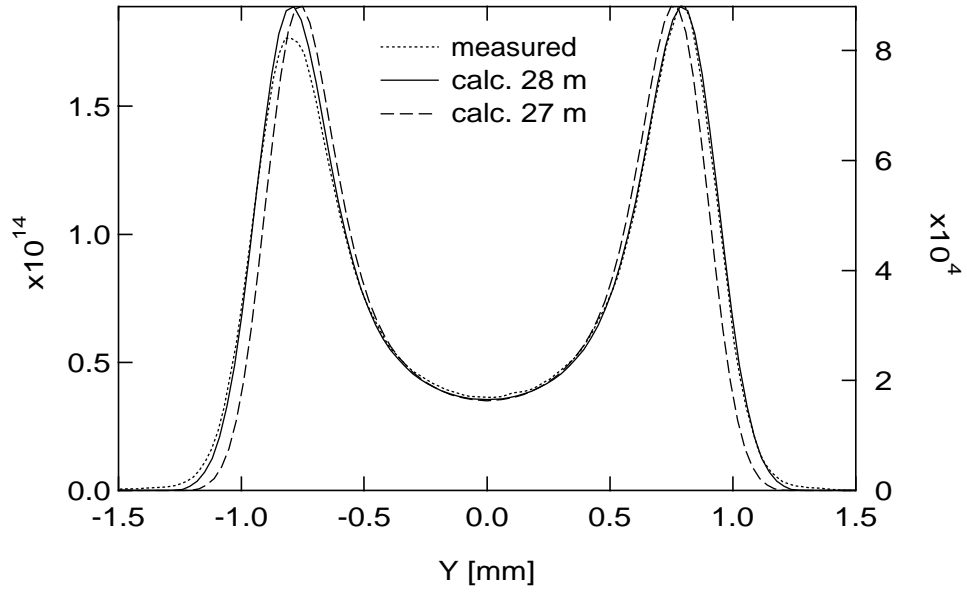


Figure 5. Measured vertical profiles at 7.3 keV (first harmonic, 18.5 mm gap) at the distances: 27 m (dashed), 28 m (solid), measured (dots).

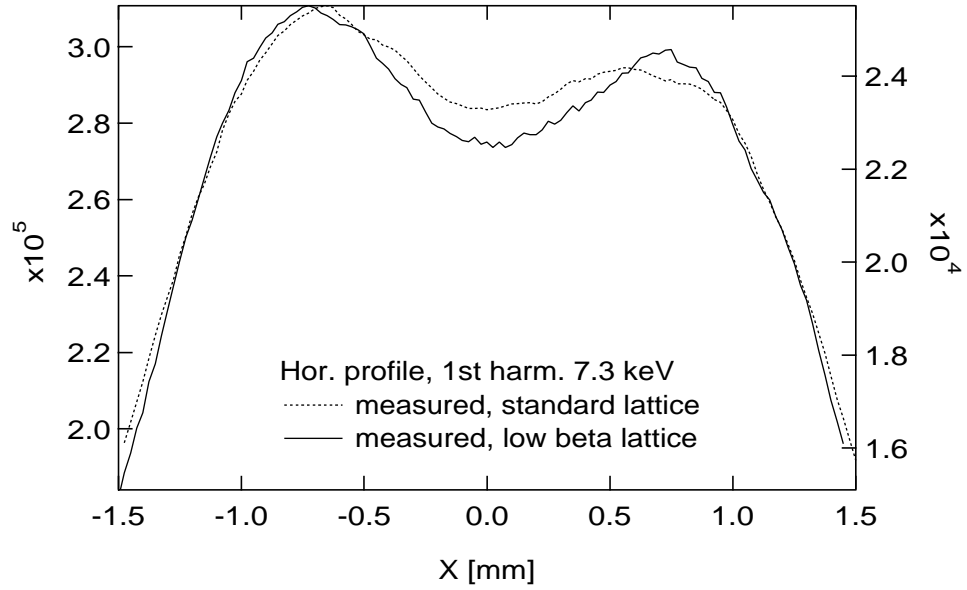


Figure 6. Measured horizontal profiles at 7.3 keV (first harmonic, 18.5 mm gap), peaks differ for the standard lattice (dashed) by 7%, low-beta lattice (solid) - 4%.

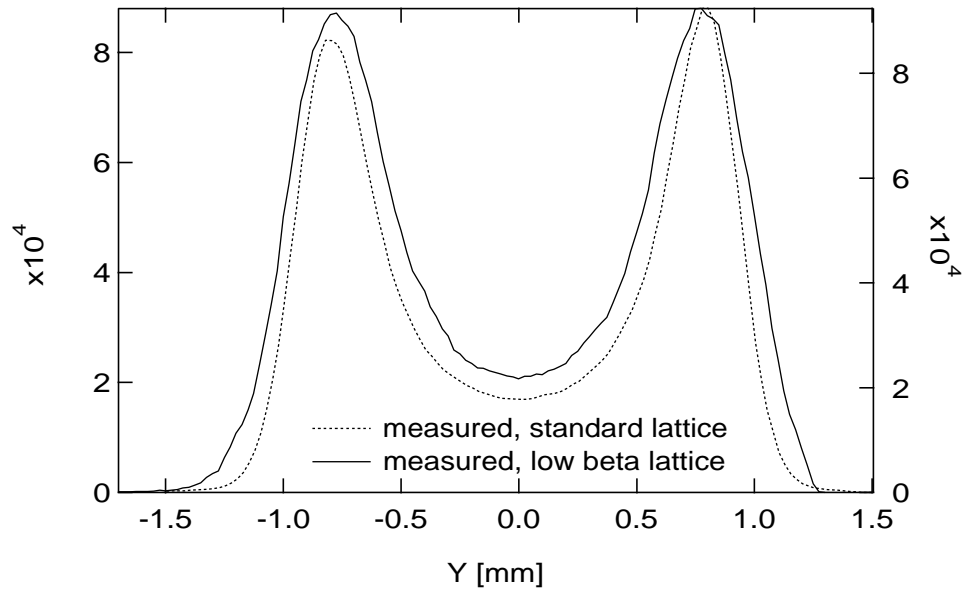


Figure 7. Measured vertical profiles at 7.3 keV (first harmonic, 18.5 mm gap), peaks differ for the standard lattice (dashed) by 7%, low-beta lattice (solid) - 1%.

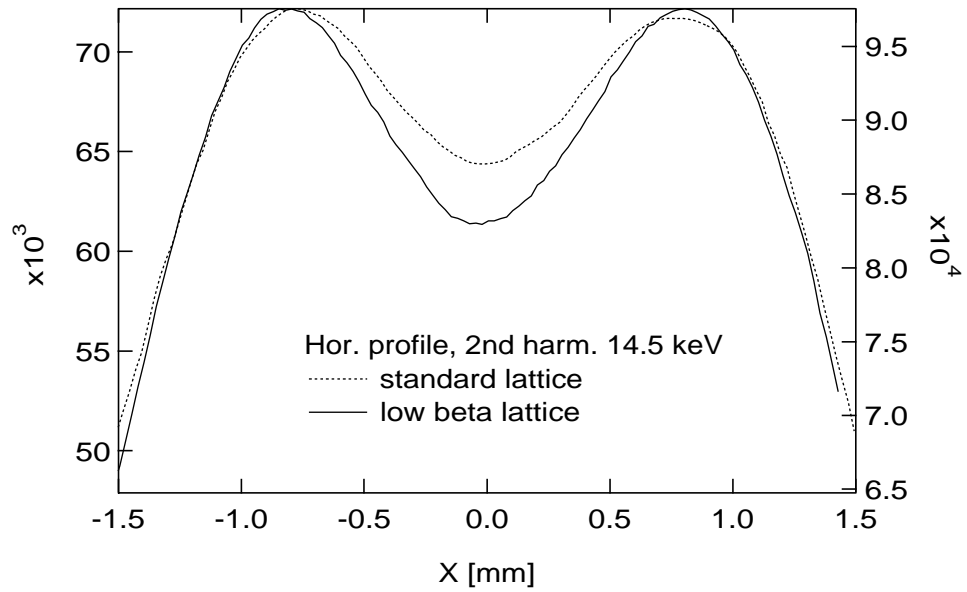


Figure 8. Measured horizontal profiles at 14.5 keV (second harmonic, 18.5 mm gap), peaks differ for the standard lattice (dashed) by 0.7%, low-beta lattice (solid).

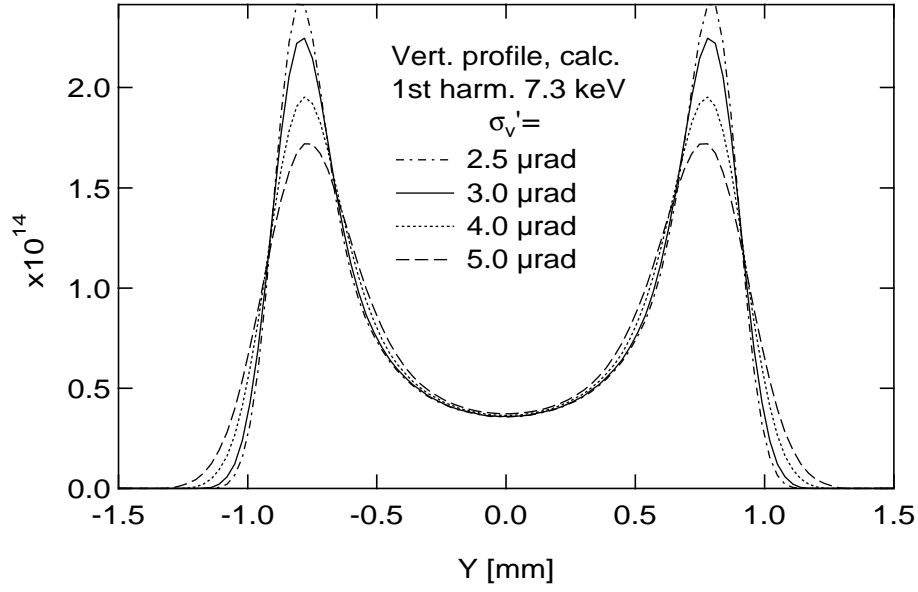


Figure 9. Calculated vertical profiles at energy 7.3 keV, $\sigma_h = 300 \mu\text{m}$, $\sigma_h' = 24 \mu\text{rad}$, $\sigma_v = 40 \mu\text{m}$, for different rms beam divergences: $\sigma_v' = 2.5$ (dash-dot), 3.0 (solid), 4.0 (dots), 5.0 (dash) μrad .

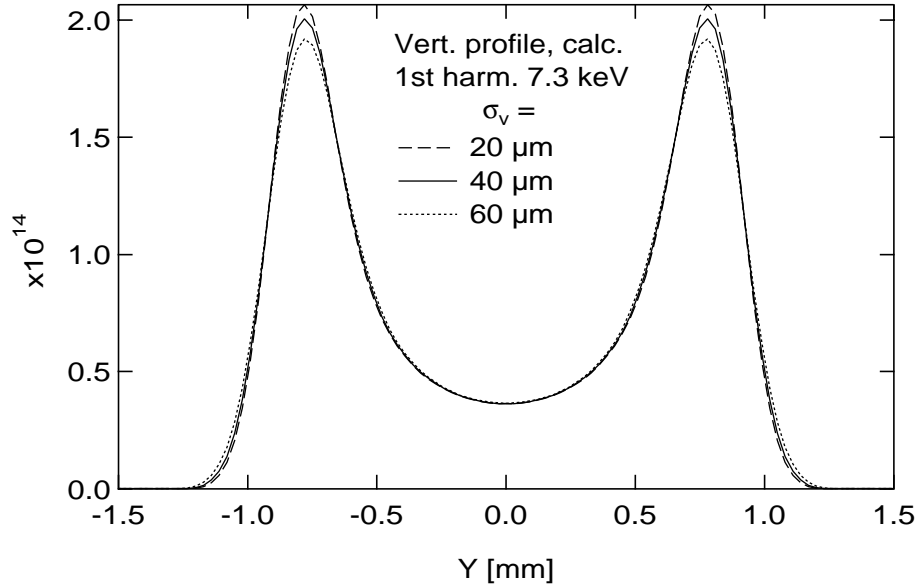


Figure 10. Calculated vertical profiles at energy 7.3 keV, $\sigma_h = 300 \mu\text{m}$, $\sigma_h' = 24 \mu\text{rad}$, $\sigma_v' = 2.5 \mu\text{rad}$, for different rms beam sizes: $\sigma_v = 20$ (dash), 40 (solid), 60 (dots) μm .

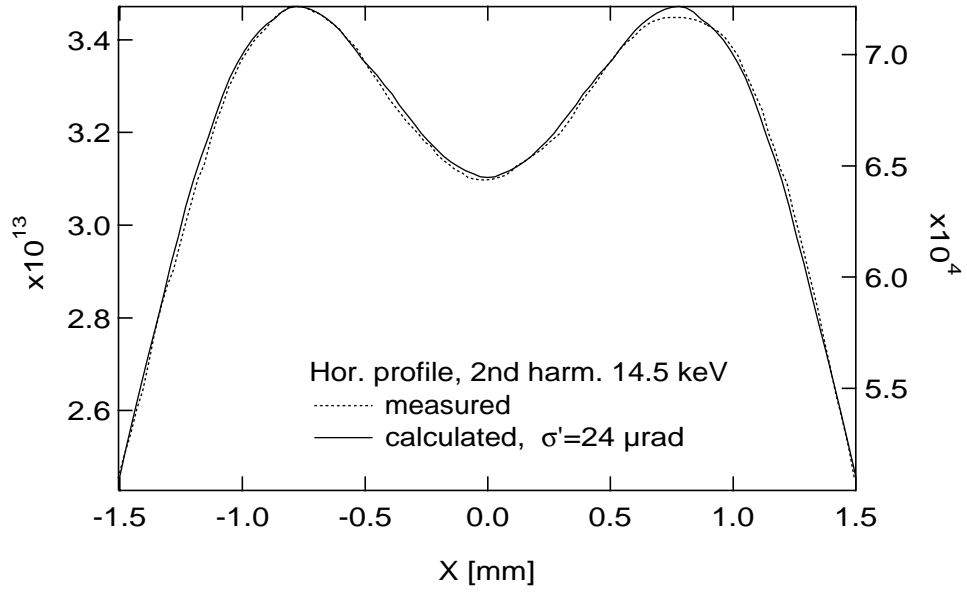


Figure 11. Horizontal profiles at 14.5 keV (second harmonic), standard lattice. Measured (dots) and calculated for $\sigma_h = 300 \mu\text{m}$, $\sigma'_h = 24.0 \mu\text{rad}$ (solid).

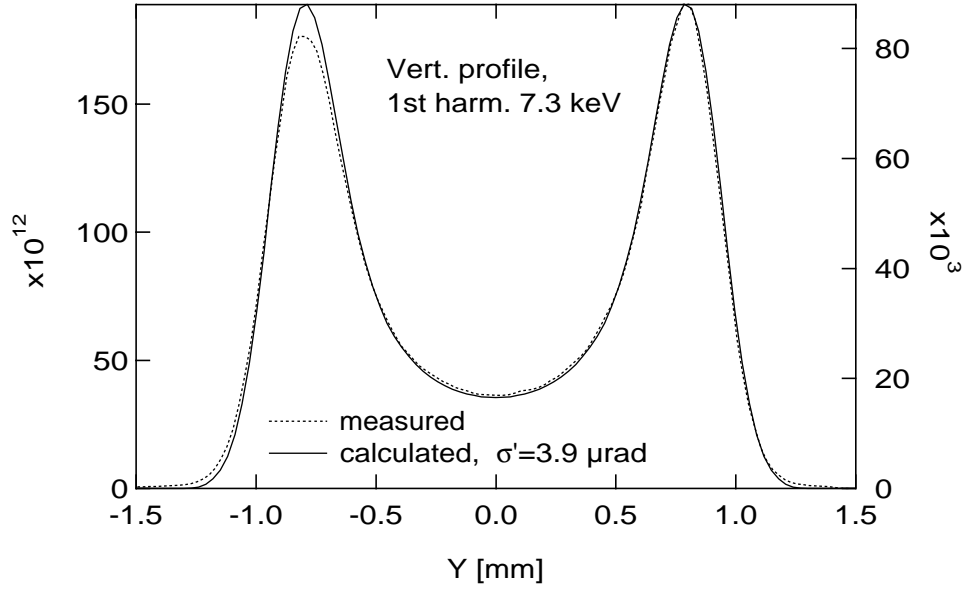


Figure 12. Vertical profiles at 7.3 keV (first harmonic) standard lattice. Measured (dots), calculated for $\sigma_v = 50 \mu\text{m}$, $\sigma'_v = 3.9 \mu\text{rad}$ (solid).

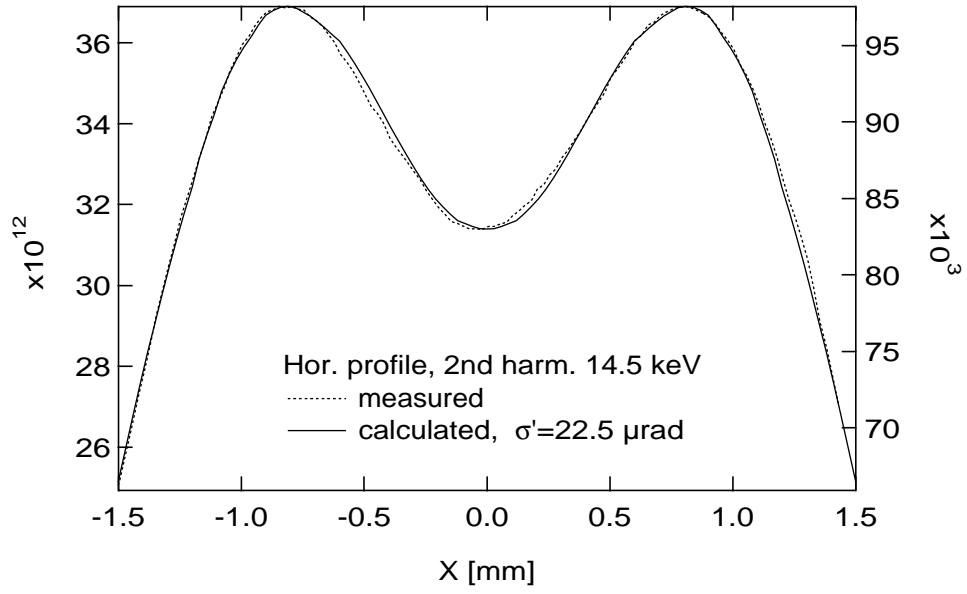


Figure 13. Horizontal profiles at 14.50 keV (second harmonic), low-beta lattice. Measured (dots), calculated for $\sigma_h = 300 \mu\text{m}$, $\sigma_h' = 22.5 \mu\text{rad}$ (solid).

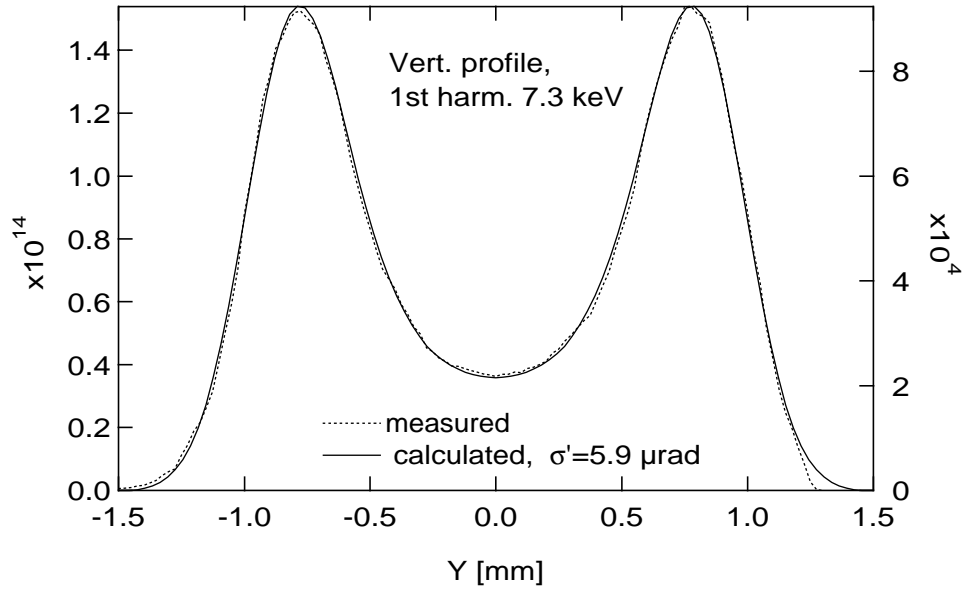


Figure 14. Vertical profiles at 7.3 keV (first harmonic) low-beta lattice. Measured (dots), calculated for $\sigma_v = 50 \mu\text{m}$, $\sigma_v' = 5.9 \mu\text{rad}$ (solid).

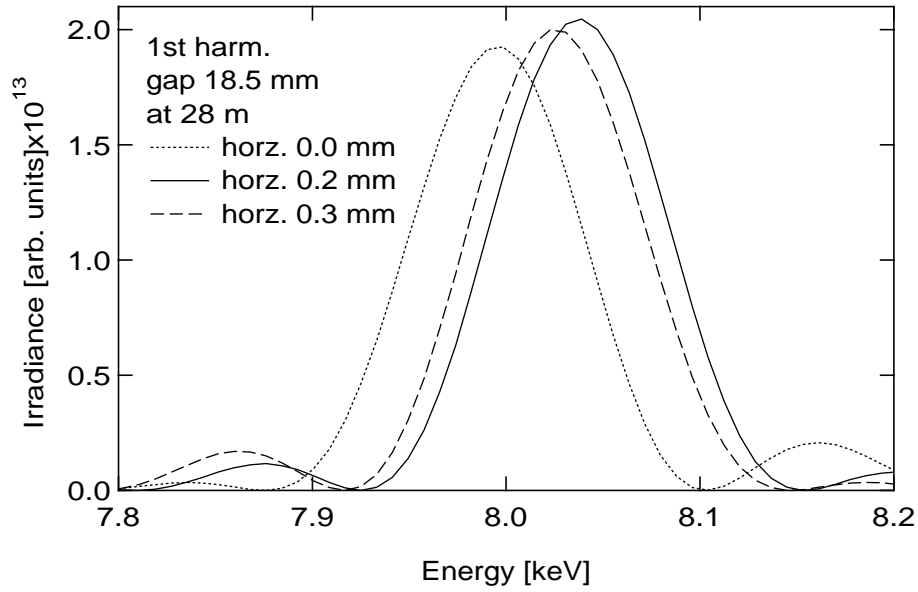


Figure 15. A single particle undulator spectrum calculation for the measured magnetic field and different horizontal directions [0.0 mm (dots), 0.2 mm (solid), 0.3 mm (dashed)] at 28 m. The undulator radiation axis corresponds to the maximum intensity and higher harmonic energy value, which is at 0.2 mm (solid).

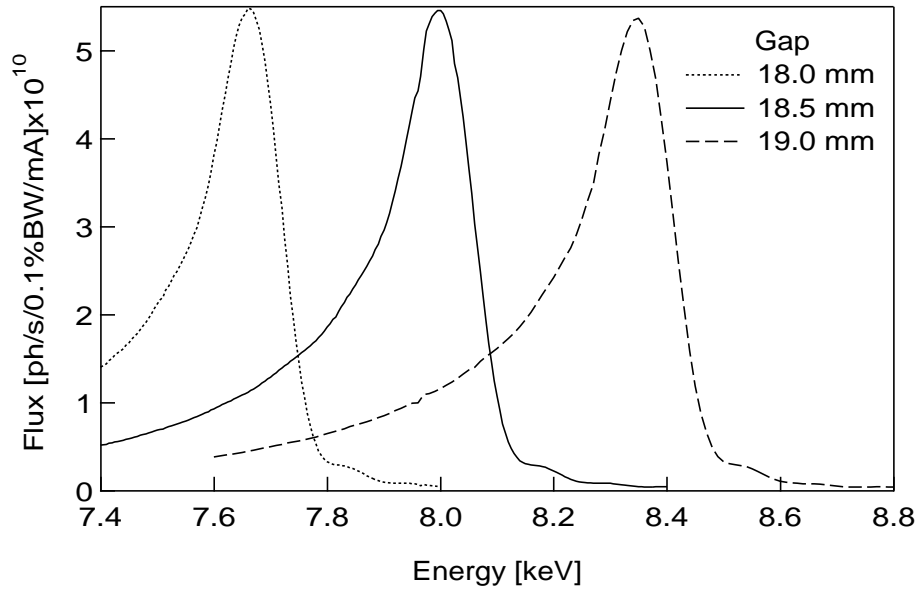


Figure 16. Measured undulator absolute flux of the first harmonic at gaps of 18.0 (dot), 18.5 (solid), 19.0 (dashed), through the 150 x 75 μm aperture at 28.0 m.

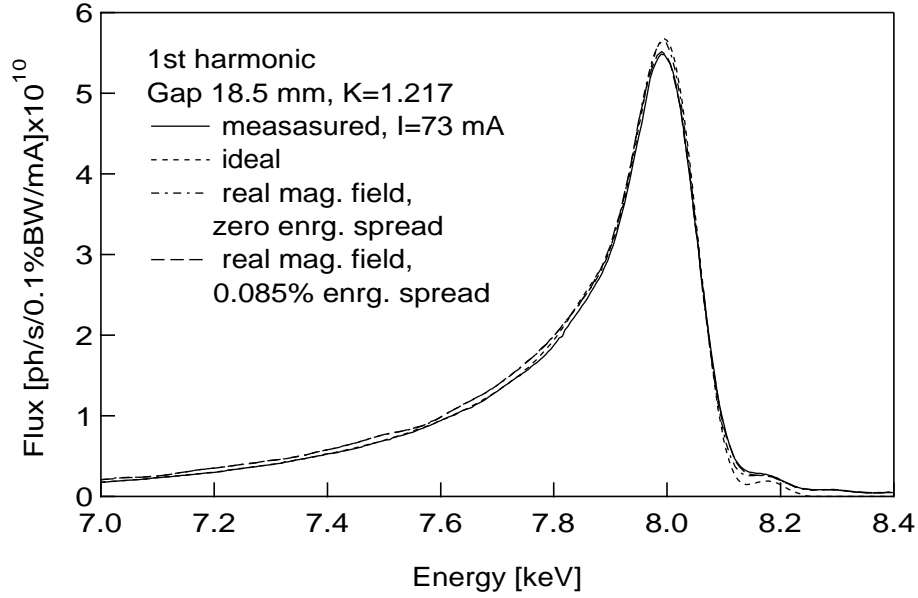


Figure 17. Undulator first harmonic absolute flux at the gap of 18.5 mm. Measured (solid), calculated through the 150 x 75 μm aperture at 28.0 m for $\sigma_h = 300 \mu\text{m}$, $\sigma_h' = 24.0 \mu\text{rad}$, for $\sigma_v = 50 \mu\text{m}$, $\sigma_v' = 3.9 \mu\text{rad}$: ideal (dots), measured mag. field and zero energy spread (dashed-dot), measured mag. field and 0.085% energy spread (dashed).

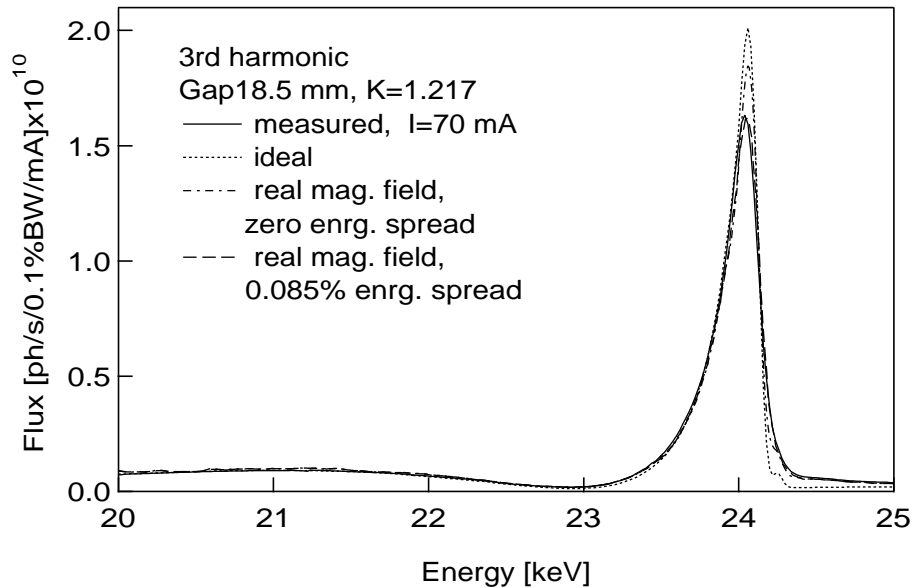


Figure 18. Undulator third harmonic absolute flux at the gap of 18.5 mm. Measured (solid), calculated through the 150 x 75 μm aperture at 28.0 m for $\sigma_h = 300 \mu\text{m}$, $\sigma_h' = 24.0 \mu\text{rad}$, for $\sigma_v = 50 \mu\text{m}$, $\sigma_v' = 3.9 \mu\text{rad}$: ideal (dots), measured mag. field and zero energy spread (dashed-dot), measured mag. field and 0.085% energy spread (dashed).

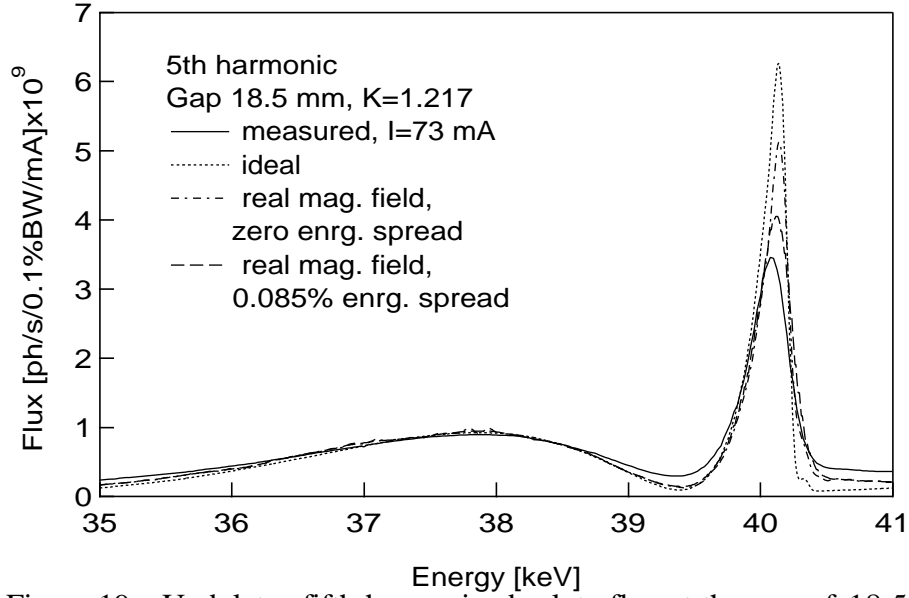


Figure 19. Undulator fifth harmonic absolute flux at the gap of 18.5 mm. Measured (solid), calculated through the $150 \times 75 \mu\text{m}$ aperture at 28.0 m for $\sigma_h = 300 \mu\text{m}$, $\sigma_h' = 24.0 \mu\text{rad}$, for $\sigma_v = 50 \mu\text{m}$, $\sigma_v' = 3.9 \mu\text{rad}$: ideal (dots), measured mag. field and zero energy spread (dashed-dot), measured mag. field and 0.085% energy spread (dashed).

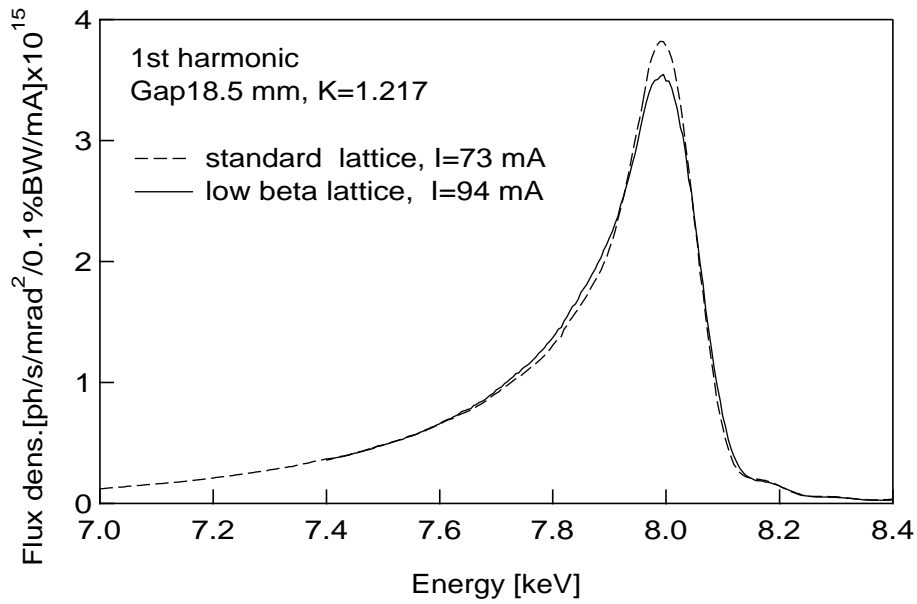


Figure 20. Measured on-axis absolute flux density of the first harmonic at a gap of 18.5 mm for the standard lattice (dashed) and low-beta lattice (solid).